Electrical injection and control of vector spin flow in altermagnets

Yanmeng Lei,[1] Rui-Chun Xiao,[2,3] Weiwei Lin,[4] and Tao Yu[1,*]
[1]*School of Physics, Huazhong University of Science and Technology, Wuhan 430074, China*
[2]*Institute of Physical Science and Information Technology, Anhui University, Hefei 230601, China*
[3]*Anhui Provincial Key Laboratory of Magnetic Functional Materials and Devices, Anhui University, Hefei 230601, China*
[4]*School of Physics, Southeast University, Nanjing 211189, China*

(Received 2 May 2026; revised 9 September 2026; accepted 21 October 2026; published 2 November 2026)

Altermagnets host chirally split magnons that promise unique functionalities for information processing. However, their distinctive transport signatures, crucial for experimental identification and manipulation, remain elusive. Here, we predict that a spin accumulation electrically injects a "vector" or multidirectional magnon spin current into an altermagnet, comprising both longitudinal and sizable transverse components. Notably, this transverse current exhibits a sign reversal away from the source and can be switched on or off by reorienting the Néel vector. While such a transverse current is found to be not forbidden even in conventional antiferromagnets, we demonstrate through quantum-kinetic calculations that, in altermagnets, the transverse response is enhanced by two orders of magnitude due to broken parity-time-translation ($PT\tau$) symmetry. This giant enhancement provides a decisive transport fingerprint for detecting magnon spin splitting and Néel-vector orientation, offering a clear criterion to experimentally distinguish nonrelativistic spin splitting from relativistic anisotropy effects.

DOI: 10.1103/4mcl-jtty

I. INTRODUCTION

Altermagnets (ATMs) constitute a distinct magnetic phase that combines the high-frequency dynamics of antiferromagnets (AFMs) with the pronounced spin-dependent responses of ferromagnets [1–6]. A key feature is a unique interplay of crystal and spin-rotation symmetries that breaks global Kramers degeneracy [2,7], producing the observed nonrelativistic spin splitting in electronic bands via x-ray magnetic circular dichroism [8–10] and angle-resolved photoemission spectroscopy [11–17].

This spin splitting enables novel spintronic effects, including nonrelativistic spin splitting torque [18], crystal Hall effect [19–21], unique magneto-optical responses [22–24], and unconventional thermal transport [25]. Moreover, ATMs host chirally split magnons [26–32] (the quanta of spin waves [33–37]), promising for low-dissipation spin transport [27,38–40]. Efficient spin transport in conventional AFMs is often hindered by magnetization compensation, requiring a large magnetic field or strong spin-orbit coupling to overcome [41–58]. ATMs intrinsically bypass this via chiral magnon splitting, enabling effects like the temperature-gradient-driven magnon spin Nernst effect [27,38,40], previously associated with magnon spin swapping in AFMs [50].

Electrical spin injection from a heavy metal is a highly efficient method to generate magnon spin currents, demonstrated for longitudinal spin flow in ferromagnets [59], ferrimagnets [60,61], and antiferromagnets [54–58]. In contrast to the thermal response [27,38,40], the electrical spin injection couples the magnon spin polarization directly to electron spin accumulation. Its behavior in altermagnetism, however, remains wanting.

In this work, we fill this gap by exploring the electrically injected, diffusion-driven transport of magnon spins in ATMs, developing a microscopic quantum kinetic equation, and performing a symmetry analysis. We demonstrate that the electron spin accumulation $\Delta\boldsymbol{\mu}$ at a heavy-metal–ATM interface produces a "vector" magnon (spin) current, i.e., multidirectional propagation containing both transverse and longitudinal magnon flows propagating normal and parallel to the spin-accumulation gradient [Figs. 1(a) and 1(b)]. Notably, the transverse part reverses its direction when flowing away from the source due to *intrinsic* differences in magnon diffusion lengths originating from different group velocities of two modes in ATMs, which can be turned on or off by reorienting the Néel vector. Surprisingly, the transverse current also exists in conventional AFMs when the Néel vector tilts away from the diffusion axis, because the in-plane uniaxial anisotropy renders the magnon dispersion anisotropic (especially at high frequencies), thereby distorting the group-velocity distribution [Fig. 1(c)]. However, in AFMs, the transverse velocities $\mathbf{v}_\perp$ of two magnon modes nearly compensate, yielding only a weak net transverse spin current. In ATMs, in contrast, magnon spin splitting from broken parity-time-translation ($PT\tau$) symmetry creates strong asymmetry between the two modes, leading to a large imbalance in transverse velocity and a greatly enhanced transverse spin current [Fig. 1(d)]. This intrinsic mechanism enhances the net transverse response in ATMs by two orders of magnitude compared to AFMs of similar crystal symmetry, offering a clear transport signature to distinguish ATMs from conventional AFMs.

*Contact author: taoyuphy@hust.edu.cn

Published by the American Physical Society under the terms of the Creative Commons Attribution 4.0 International license. Further distribution of this work must maintain attribution to the author(s) and the published article's title, journal citation, and DOI.

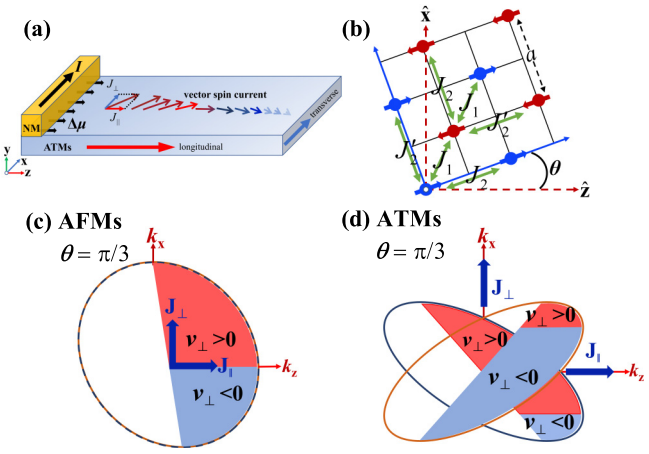


FIG. 1. Diffusive magnon spin transport in ATMs vs AFMs under electrical injection. (a) A charge current $I\hat{\mathbf{x}}$ in the normal metal (NM) creates a spin accumulation $\Delta\boldsymbol{\mu} \parallel \hat{\mathbf{z}}$ via spin Hall effect, driving a vector magnon flow in ATMs. Red and blue arrows indicate the reversed transverse flow. (b) Minimal ATMs model with the Néel vector $\mathbf{n}$ forming an angle θ to the diffusion $\hat{\mathbf{z}}$ axis. (c), (d) Transverse magnon flow in AFMs and ATMs when $\mathbf{n} \nparallel \hat{\mathbf{z}}$. Red (blue) denotes positive (negative) transverse group velocities $\mathbf{v}_\perp \parallel \hat{\mathbf{x}}$ of injected magnons.

II. MODEL AND SYMMETRY

We model the ATMs using a minimal square-lattice model with lattice constant a, shown in Fig. 1(b). The spin Hamiltonian reads

$$\begin{aligned}\hat{H} = {} & J_1 \sum_{\langle i,j\rangle} \hat{\mathbf{S}}_{1,i} \cdot \hat{\mathbf{S}}_{2,j} - \gamma\hbar \sum_i \mathbf{H}_0 \cdot (\hat{\mathbf{S}}_{1,i} + \hat{\mathbf{S}}_{2,i}) \\ & + J_2 \sum_{\langle i_z, j_z\rangle} \hat{\mathbf{S}}_{1,i} \cdot \hat{\mathbf{S}}_{1,j} + J_2' \sum_{\langle i_x, j_x\rangle} \hat{\mathbf{S}}_{1,i} \cdot \hat{\mathbf{S}}_{1,j} \\ & + J_2' \sum_{\langle i_z, j_z\rangle} \hat{\mathbf{S}}_{2,i} \cdot \hat{\mathbf{S}}_{2,j} + J_2 \sum_{\langle i_x, j_x\rangle} \hat{\mathbf{S}}_{2,i} \cdot \hat{\mathbf{S}}_{2,j} \\ & + K \sum_i \left(\hat{\mathbf{S}}_{1,i}^z\right)^2 + K \sum_i \left(\hat{\mathbf{S}}_{2,i}^z\right)^2. \end{aligned} \tag{1}$$

Here, $\hat{\mathbf{S}}_{1,i}$ and $\hat{\mathbf{S}}_{2,j}$ represent spins of magnitude S on *occupied* lattice sites of sublattices 1 and 2. $\langle i, j\rangle$ denotes the nearest-neighbor coupling between different sublattices along the diagonal direction of the square lattice, while $\langle i_x, j_x\rangle$ and $\langle i_z, j_z\rangle$ indicate the nearest-neighbor coupling of the same sublattice along two main axis of the crystal. $J_1 > 0$ is the antiferromagnetic intersublattice exchange constant, J_2 (J_2') is the intrasublattice exchange constant, $K < 0$ is uniaxial anisotropy constant, γ is the electron gyromagnetic ratio, and $\mathbf{H}_0$ is the applied magnetic field aligned with the Néel vector $\mathbf{n}$. To realize different spin-injection configurations with different relative directions of $\mathbf{n}$ and $\Delta\boldsymbol{\mu}$, fabrication of a series of heavy-metal strips atop an altermagnet film is convenient since the measurements can be compared easily without introducing artificial factors. In the calculation, this is equivalent to treat the Néel vector tunable and forms an angle θ with the diffusion $\hat{\mathbf{z}}$ direction [Fig. 1(b)].

The dispersions $\omega_{1/2,\mathbf{k}}(\theta)$ of modes 1 and 2 are chirally split, carrying opposite spins $-\hbar$ and $+\hbar$ along the Néel vector (see Supplemental Material (SM) [62] for details). The existence of the parity-effective-time operation $PTC_x(\pi)$ ($C_x(\pi)$ is a global π spin rotation about the $\hat{\mathbf{x}}$ axis) in collinear magnets does not protect band degeneracy [63]. The breaking of $PT\tau$ (τ is a translation of half a unit cell along the diagonal direction) symmetry by $J_2 \neq J_2'$ causes momentum-dependent spin splitting. The magnon chirality splitting vanishes when $J_2 = J_2'$, reducing to conventional AFMs.

III. QUANTUM KINETIC THEORY

We develop the microscopic quantum kinetic equations to account for the electrical injection, coherence, diffusion, and dephasing of magnon spin current in ATMs/AFMs in the geometry [Fig. 1(a)]. Magnons in the ATMs couple with the conduction electrons in normal metal via the interfacial s–d exchange interaction [53,64–68] $\hat{H}_{\rm int} = \mathcal{J}a^3 \sum_l \sum_{i\in{\rm int}}^N \int d\mathbf{r}\delta(\mathbf{r} - \mathbf{R}_{l,i})\hat{\mathbf{s}}(\mathbf{r}) \cdot \hat{\mathbf{S}}_{l,i}$, where $\mathcal{J}$ is the exchange coupling strength, $\hat{\mathbf{s}}(\mathbf{r})$ is the electron spin density, and N is the number of interface sites. This interaction leads to the interfacial scattering between electron operator $\{\hat{c}_{\mathbf{k}\zeta}^\dagger, \hat{c}_{\mathbf{k}\chi}\}$ and magnon operator $\hat{b}_{\xi,\mathbf{q}}$ according to

$$\begin{aligned}\hat{H}_{\rm int} = {} & \frac{a}{d}\sqrt{\frac{S}{2N}}\mathcal{J} \sum_{\zeta,\chi=\uparrow,\downarrow} \sum_{\mathbf{k},\mathbf{k}'} \sum_{\mathbf{q}} \sum_{\xi=1,2} \left(\boldsymbol{\sigma}_{\zeta\chi} \cdot \delta\mathbf{S}_{\mathbf{q}}^{\xi}\right) \\ & \times \hat{c}_{\mathbf{k}'\zeta}^\dagger \hat{c}_{\mathbf{k}\chi} \hat{b}_{\xi,\mathbf{q}} \delta_{\mathbf{k}+\mathbf{q},\mathbf{k}'} + {\rm H.c.}, \end{aligned} \tag{2}$$

where d is the thickness of NM and $\boldsymbol{\sigma}$ is the Pauli matrices. The scattering amplitude for electron-magnon processes is captured by the kernel

$$\boldsymbol{\sigma} \cdot \delta\mathbf{S}_{\mathbf{q}}^{\xi=1,2} \sim \begin{pmatrix} -\sin\theta & \cos\theta \mp 1 \\ \cos\theta \pm 1 & \sin\theta \end{pmatrix}, \tag{3}$$

which depends on the orientation θ of the Néel vector $\mathbf{n}$. The interfacial disorder can be incorporated in the formalism as well, which only suppresses the efficiency slightly (see Appendix A). When $\theta = 0$ (i.e., $\mathbf{n} \parallel \hat{\mathbf{z}}$), only the off-diagonal $\zeta \neq \chi$ elements are nonzero in Eq. (3), indicating that magnon scattering induces spin flips of the electrons—for instance, absorption of a mode-1 magnon flips an electron from spin-up to spin-down. When $\theta = \pi/2$ ($\mathbf{n} \perp \hat{\mathbf{z}}$), all the matrix elements in Eq. (3) present with the same magnitude, allowing both spin-conserving and spin-flip processes to occur and interfere. This interference ultimately suppresses the magnon spin current (see SM [62] and the calculation below). For an arbitrary θ, this interference is not balanced, leading to a vector spin current with multidirectional flow.

We verify these expectations by modeling the magnon injection driven by a spin accumulation $\Delta\mu = \delta\mu_\uparrow - \delta\mu_\downarrow$ polarized along $\hat{\mathbf{z}}$. Under electrical injection and dissipation, the magnon density matrix $\rho_{\mathbf{q}}$, in which the diagonal terms represent magnon population and the off-diagonal terms denote the mode correlation [53], obeys the quantum kinetic equation

$$\partial_t \rho_{\mathbf{q}} = \partial_t \rho_{\mathbf{q}}|_{\rm inj} + \partial_t \rho_{\mathbf{q}}|_{\rm coh} + \partial_t \rho_{\mathbf{q}}|_{\rm rex}. \tag{4}$$

The dispersion $\mathcal{E}_{\mathbf{q}} = \mathrm{diag}(\hbar\omega_{1,\mathbf{q}}, \hbar\omega_{2,\mathbf{q}}, \hbar\omega_{1,-\mathbf{q}}, \hbar\omega_{2,-\mathbf{q}})$ of magnons drives the coherent dynamics of nonequilibrium magnons according to

$$\partial_t \rho_{\mathbf{q}}|_{\mathrm{coh}} = (-i/\hbar)(\rho_{\mathbf{q}}\sigma_3\mathcal{E}_{\mathbf{q}} - \mathcal{E}_{\mathbf{q}}\sigma_3\rho_{\mathbf{q}}), \tag{5}$$

where $\sigma_3 = \mathrm{diag}(1, 1, -1, -1)$ is the metric. Within the relaxation-time approximation [69,70], the magnons relax toward to their equilibrium $\rho_{\mathbf{q}}^{(0)}$ by

$$\partial_t \rho_{\mathbf{q}}|_{\mathrm{rex}} = -\big(\rho_{\mathbf{q}} - \rho_{\mathbf{q}}^{(0)}\big)/\tau_m, \tag{6}$$

with a characteristic time τ_m assumed equal for both modes [71]. The spin accumulation drives the electrical injection as described by

$$\partial_t \rho_{\mathbf{q}}|_{\mathrm{inj}} = \frac{\pi}{\hbar}\frac{S}{2N}\frac{a^2}{d^2}\mathcal{J}^2 \sum_{\mathbf{k}} \sum_{\zeta,\chi=\uparrow,\downarrow} [f_{\mathbf{k}+\mathbf{q},\zeta}(1 - f_{\mathbf{k},\chi})(\sigma_3 + \rho_{\mathbf{q}}) - f_{\mathbf{k},\chi}(1 - f_{\mathbf{k}+\mathbf{q},\zeta})\rho_{\mathbf{q}}]\mathcal{M}_{\zeta\chi}(\mathbf{k}, \mathbf{k}+\mathbf{q}) + \mathrm{H.c.}, \tag{7}$$

where $f_{\mathbf{k},\zeta} = [f_{\mathbf{k}}^0 - (\partial f_{\mathbf{k}}^0/\partial\varepsilon_{\mathbf{k}})\delta\mu_\zeta]$ is its nonequilibrium distribution for spin ζ (shifted from the equilibrium Fermi-Dirac distribution $f_{\mathbf{k}}^0$), $\varepsilon_{\mathbf{k}}$ is the electron kinetic energy, and $\mathcal{M}_{\zeta\chi}(\mathbf{k}, \mathbf{k}+\mathbf{q})$ is a 4×4 matrix encoding all the electron-magnon scattering processes in Eq. (3) (see SM [62] for details).

The injected magnons around the source located at $z = 0$ in the setup [Fig. 1(a)] diffuse along $\hat{\mathbf{z}}$. Only the diagonal components $\rho_{11}(\mathbf{q})$ and $\rho_{22}(\mathbf{q})$ of $\rho_{\mathbf{q}}$ carry spins, which diffuse when away from the source according to

$$-v_\eta^{\parallel}(\mathbf{q})\frac{\partial\rho_{\eta\eta}(z,\mathbf{q})}{\partial z} - \frac{\rho_{\eta\eta}(z,\mathbf{q}) - \rho_{\eta\eta}^{(0)}(\mathbf{q})}{\tau_m} = 0, \tag{8}$$

where $\eta = \{1, 2\}$ indicate the modes. Solving Eq. (8) yields the magnon distribution at the region $z > 0$: when $v_\eta^{\parallel}(\mathbf{q}) > 0$, $\rho_{\eta\eta}(z,\mathbf{q}) = \rho_{\eta\eta}^{(0)}(\mathbf{q}) + [\rho_{\eta\eta}(\mathbf{q}) - \rho_{\eta\eta}^{(0)}(\mathbf{q})]e^{-z/(v_\eta^{\parallel}(\mathbf{q})\tau_m)}$; when $v_\eta^{\parallel}(\mathbf{q}) < 0$, $\rho_{\eta\eta}(z,\mathbf{q}) = \rho_{\eta\eta}^{(0)}(\mathbf{q})$. They contribute to the spin-current density

$$J_i^\alpha(z) = \frac{1}{S_0}\sum_{\eta=1,2}\sum_{\mathbf{q}}\big(\mathcal{S}_\eta^\alpha(\mathbf{q}) \otimes \mathbf{v}_\eta^i(\mathbf{q})\rho_{\eta\eta}(z,\mathbf{q})\big), \tag{9}$$

where S_0 is the area of the magnet, the superscript $\alpha = \{x, z\}$ is the spin-polarization direction, the subscript $i = \{\parallel, \perp\}$ represents the longitudinal/transverse flow direction, and $\mathcal{S}_{1/2}(\mathbf{q}) = \mp\sin\theta\hat{\mathbf{x}} \mp \cos\theta\hat{\mathbf{z}}$ is the magnon spin.

IV. ELECTRICALLY INJECTED VECTOR SPIN CURRENT

The calculation is performed using realistic material parameters: $J_1 = 12.25$ meV, $J_2 = -1.91$ meV, $J_2' = 6.20$ meV, $K = -0.07$ meV, $S = 3/2$, lattice constant $a = 0.412$ nm, possible for Cr_2I_2O [27], and NM thickness $d = 3$ nm [46,57]. Similar phenomena may be expected in other candidates, e.g., $LuFeO_3$ [40] and MnTe [12,72]. The other parameters are chosen as $\Delta\mu = 2$ meV [64,73–75], relaxation time $\tau_m = 1$ ns, and interfacial exchange coupling $\mathcal{J} = 50$ meV [65,66,76,77].

Recall that a temperature gradient drives no magnon spin current in AFMs without applied magnetic fields due to the magnetization compensation [41,45,47,49]. In contrast, electric injection generates a longitudinal spin current in AFMs (for $J_2 = J_2'$) when $\mathbf{n} \parallel \hat{\mathbf{z}}$ by selectively absorbing mode-1 magnons and injecting mode-2 magnons [43,57,78]. Figures 2(a) and 2(b) illustrate the injected magnon distribution in the Brillouin zone for ATMs, in which different group velocities of the two modes further enhance the spin current. When the Néel vector deviates from the diffusion $\hat{\mathbf{z}}$ direction, e.g., at $\theta = \pi/3$, the injected magnon distribution becomes tilted, as shown in Figs. 2(c) and 2(d). Only injected magnons with $\mathbf{v}_\parallel > 0$ contribute to the spin current at $z > 0$. Among these, the proportions with $\mathbf{v}_\perp > 0$ and $\mathbf{v}_\perp < 0$ become unbalanced: More magnons with $\mathbf{v}_\perp > 0$ are absorbed for mode 1 [Fig. 2(c)], while more with $\mathbf{v}_\perp < 0$ are injected for mode 2 [Fig. 2(d)]. This imbalance produces a large transverse magnon spin flow. When $\theta = \pi/2$, Eq. (3) implies that all electron-magnon scattering amplitudes are equal in magnitude, so spin-conserving and spin-flip processes occur with equal probability and interfere, resulting in zero net magnon injection for both modes (see SM [62]).

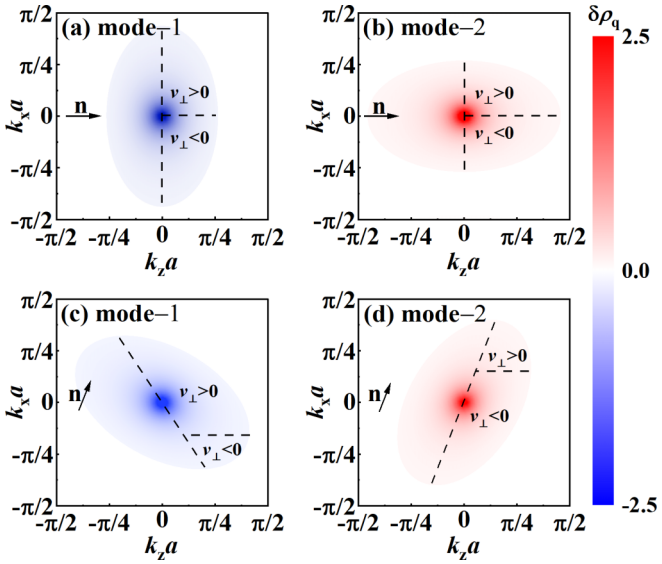


FIG. 2. Injected Bose-Einstein distribution of magnons $\delta\rho_{\mathbf{q}}$ of modes 1 and 2 under different Néel-vector directions $\theta = \{0, \pi/3\}$. (a) Mode 1 and (b) mode 2 for $\theta = 0$. (c) Mode 1 and (d) mode 2 for $\theta = \pi/3$. The plotted quantity is dimensionless.

This dependence of electrical injection on the Néel-vector orientation governs the magnon spin flow below the NM at $z \gtrsim 0$, as summarized in Figs. 3(a)–3(d). The longitudinal components $J_\parallel^z$ and $J_\parallel^x$ exhibit twofold and fourfold symmetries, while the transverse components $J_\perp^z$ and $J_\perp^x$ display double fourfold symmetries. All components vanish when $\mathbf{n} \perp \hat{\mathbf{z}}$ due to vanishing magnon injection, and the transverse components vanish for $\mathbf{n} \parallel \hat{\mathbf{z}}$ because transverse velocities cancel [Figs. 2(a) and 2(b)]. Transverse components also vanish at $\theta = \{\pi/4, 3\pi/4, 5\pi/4, 7\pi/4\}$, where contributions from the two magnon modes precisely offset each other. Crucially, the AFMs exhibit similar features but with a strongly suppressed transverse current. Therefore, clear experimental evidence rests on the transverse-to-longitudinal ratio, which is two orders of magnitude larger in ATMs than in AFMs. Here, the ratio of the exchange anisotropy to the uniaxial anisotropy

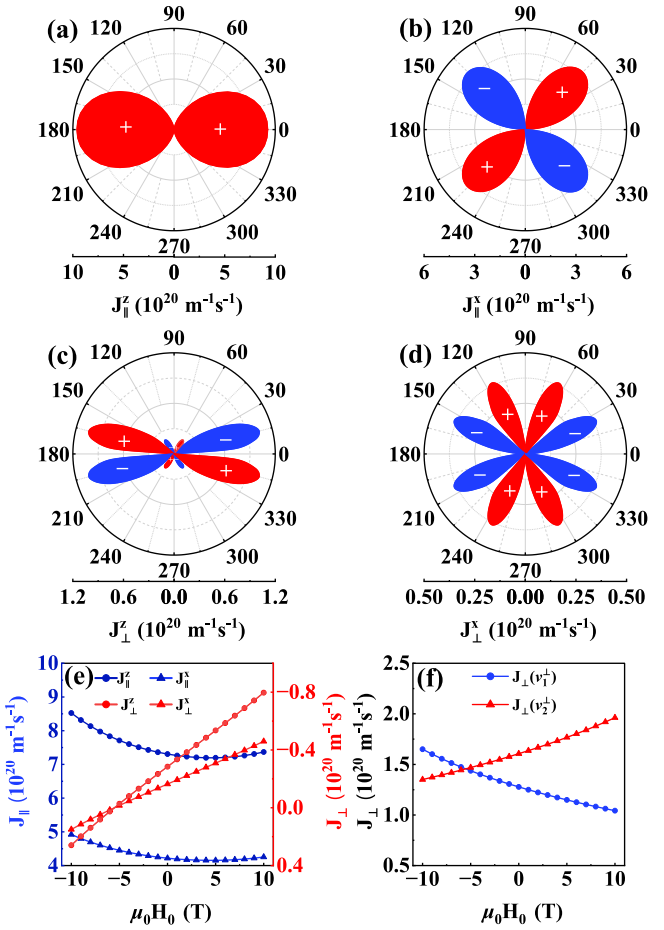


FIG. 3. Dependence on the Néel-vector orientation θ at $z \gtrsim 0$ of the longitudinal magnon spin currents with spin polarization along $\hat{\mathbf{z}}$ [panel (a): $J_\parallel^z$] and $\hat{\mathbf{x}}$ [panel (b): $J_\parallel^x$] and the transverse magnon spin currents with spin polarization along $\hat{\mathbf{z}}$ [panel (c): $J_\perp^z$] and $\hat{\mathbf{x}}$ [panel (d): $J_\perp^x$]. Panels (e) and (f) illustrate efficient control of these spin currents by the applied magnetic field at $\theta = \pi/6$.

$|(J_2 - J_2')/K|$ provides a criterion for judging the relative magnitude of the transverse response of uniaxial ATMs and AFMs (see Appendix B). Electrical injection exhibits symmetries completely distinct from longitudinal ($A_3 \cos^2\theta + B_3 \sin^2\theta$) and transverse ($\sin\theta\cos\theta$) spin currents driven by a temperature gradient (see Appendix C).

V. SYMMETRY ANALYSIS

This clear dependence on the Néel-vector orientation of the vector magnon spin flow suggests that its generation and transport under electrical injection beneath the heavy metal is governed by symmetry and dynamical constraints. The magnon spin flow J_i^α near the heavy metal is related to the spin-accumulation gradient $\delta\mu_j^\beta$ of electrons with gradient j direction and spin-polarization β direction via the fourth-order tensor $\Gamma_{ij}^{\alpha\beta}$ according to

$$J_i^\alpha = \Gamma_{ij}^{\alpha\beta}\delta\mu_j^\beta. \tag{10}$$

In J_i^α and $\Gamma_{ij}^{\alpha\beta}$, the subscripts $\{i, j\} \in \{x, z\}$ denote flow directions, while the superscripts $\{\alpha, \beta\} \in \{x, z\}$ specify spin-polarization orientations. In the geometry [Fig. 1(a)], $\beta = z$ is the spin-polarization direction, while $j = z$ is the spin-accumulation gradient direction. Our microscopic calculation reveals that all components of $\Gamma_{ij}^{\alpha\beta}$ are allowed in ATMs and AFMs, implying that a transverse magnon spin current flowing along x can emerge in either system.

TABLE I. Transformation of response tensor $\Gamma_{ij}^{\alpha\beta}$ and Néel vector under mirror operations $\{\mathcal{M}_x, \mathcal{M}_z\}$.

Elements	$\mathcal{M}_x$	$\mathcal{M}_z$
Γ_{zz}^{zz}	Γ_{zz}^{zz}	Γ_{zz}^{zz}
Γ_{zz}^{xz}	$-\Gamma_{zz}^{xz}$	$-\Gamma_{zz}^{xz}$
Γ_{xz}^{zz}	$-\Gamma_{xz}^{zz}$	$-\Gamma_{xz}^{zz}$
Γ_{xz}^{xz}	Γ_{xz}^{xz}	Γ_{xz}^{xz}
n_x	$-n_x$	n_x
n_z	n_z	$-n_z$

As the Néel vector $\mathbf{n}$ rotates in the film xz plane, the magnon spin current evolves accordingly. Consequently, the response tensor $\Gamma_{ij}^{\alpha\beta}$ is assumed to be expanded as a series in the components of $\mathbf{n} = (n_x, 0, n_z)$ [79,80]. Because J_i^α is invariant under the Néel-vector reversal ($\mathbf{n} \to -\mathbf{n}$), only even-order terms appear in the expansion. A further dynamical constraint requires the magnon spin current to vanish when $\mathbf{n}$ is perpendicular to the spin-accumulation polarization. For interpreting, we consider two mirror operations $\mathcal{M}_x$ and $\mathcal{M}_z$ with respect to the x-y and y-z planes. The transformation of the response tensor and the Néel vector is summarized in Table I (see SM [62] for details). Subsequent symmetry operations determine the explicit dependence of the tensor components on $\mathbf{n}$, as summarized in Table II (see SM [62] for details). Microscopic model calculations yield the expansion coefficients: While the longitudinal coefficients are nearly identical between ATMs and AFMs ($A_1 \approx A_2$, $B_1 \approx B_2$), the transverse coefficients in ATMs are strongly enhanced, exceeding those in AFMs by almost two orders of magnitude ($C_1 \approx 60C_2$, $D_1 \approx 60D_2$, and $E_1 \approx 60E_2$).

VI. TUNABILITY OF VECTOR SPIN CURRENT

The magnetic field along the Néel vector efficiently controls spin currents [Fig. 3(e)]. The longitudinal components $J_\parallel^{z,x}(H_0) \approx J_\parallel^{z,x}(-H_0)$ are nearly symmetric about $H_0 = 0$, while the transverse components are asymmetric. This asymmetry arises from opposite frequency shifts of two magnon

TABLE II. Dependence of response tensor $\Gamma_{ij}^{\alpha\beta}$ on the Néel vector $(n_x, 0, n_z) = (\sin\theta, 0, \cos\theta)$ in ATMs and AFMs. $\{A_{1,2}, B_{1,2}, C_{1,2}, D_{1,2}, E_{1,2}\}$ are the expansion coefficients.

	ATMs	AFMs
Γ_{zz}^{zz}	$A_1 \cos^2\theta$	$A_2 \cos^2\theta$
Γ_{zz}^{xz}	$B_1 \sin\theta\cos\theta$	$B_2 \sin\theta\cos\theta$
Γ_{xz}^{zz}	$C_1 \sin 2\theta + D_1 \sin 4\theta$	$C_2 \sin 2\theta + D_2 \sin 4\theta$
Γ_{xz}^{xz}	$E_1 (\cos 2\theta - \cos 6\theta)$	$E_2 (\cos 2\theta - \cos 6\theta)$

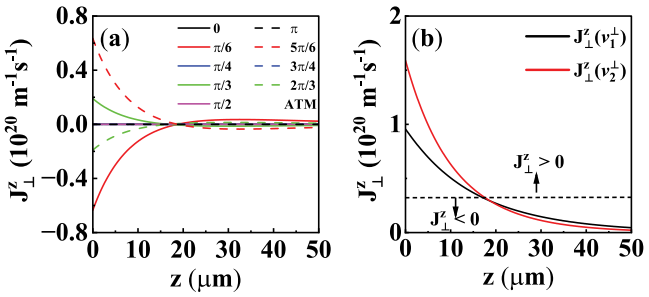


FIG. 4. (a) Transverse spin current $J_\perp^z$ as a function of the propagation distance z for different orientations θ of the Néel vector. (b) Spatial profiles of the mode-resolved contributions $J_\perp^z(v_1^\perp)$ and $J_\perp^z(v_1^\perp)$ at $\theta = \pi/6$.

modes: increasing H_0 up-shifts mode-1 frequency, reducing magnon absorption, while down-shifting mode-2 frequency enhances magnon generation, and vice versa. Therefore, the magnon current carried by the two modes, $J_\perp(v_1^\perp)$ and $J_\perp(v_2^\perp)$, depends oppositely on the magnetic field [Fig. 3(f)], thus explaining the H_0 dependence of net transverse current $J_\perp = J_\perp(v_1^\perp) - J_\perp(v_2^\perp)$.

The spatial evolution of the transverse spin current $J_\perp^z$ exhibits a nontrivial sign reversal at a finite distance, as shown in Fig. 4(a), indicating a reorientation of the vector current. This behavior originates from the unequal decay rates of the two magnon modes. For example, at $\theta = \pi/6$ [Fig. 4(b)], the contribution of mode-1 $J_\perp^z(v_1^\perp)$ is smaller at $z = 0$ but decays slowly, while $J_\perp^z(v_2^\perp)$ is larger initially but decays rapidly. Consequently, the net transverse current reverses at a finite propagation distance.

VII. SUMMARY

In summary, we introduce the concept of "vector magnonics" by showing that electrical spin injection drives a vector magnon spin current—with both longitudinal and transverse components—in ATMs and AFMs, which can laterally connect different spintronic units on a chip. This current is electrically controllable via the Néel vector or spin-accumulation orientation. A key quantum signature is the spatial reversal of the transverse flow direction, arising from interference and unequal decay between two chirally split magnon modes. Crucially, our combined microscopic and symmetry analysis reveals that the transverse-to-longitudinal spin-current ratio is enhanced by two orders of magnitude in ATMs compared with AFMs when the $PT\tau$ symmetry is strongly broken with the ratio $|(J_2 - J_2')/K| \sim 100$. This giant ratio provides an experimental fingerprint to distinguish nonrelativistic spin splitting from relativistic anisotropy effects and offers a much-needed transport probe for insulating ATMs, complementing the spectroscopic probe of magnon spin splitting [10,24,30].

ACKNOWLEDGMENTS

This work was financially supported by the National Key Research and Development Program of China under Grant No. 2023YFA1406600 and the National Natural Science Foundation of China under Grants No. 12374109 and No. 12474100.

DATA AVAILABILITY

The data that support the findings of this article are not publicly available upon publication because it is not technically feasible and/or the cost of preparing, depositing, and hosting the data would be prohibitive within the terms of this research project. The data are available from the authors upon reasonable request.

APPENDIX A: ROLE OF INTERFACIAL DISORDER IN THE SPIN INJECTION

We extend our theory beyond the ideal lattice-matched limit to realistic interfaces by introducing interfacial disorder in our formalism following Ref. [81]. Here, interface disorder renders the momentum not strictly conserved in the electric spin injection process, so we replace the momentum-conservation $\delta_{\mathbf{k}+\mathbf{q},\mathbf{k}'}$ with an interface-disorder form factor

$$F_{\mathbf{k},\mathbf{k}',\mathbf{q}} = \frac{1}{2\pi\sigma^2}\exp\left[-\frac{(\mathbf{k}'-\mathbf{k}-\mathbf{q})^2}{2\sigma^2}\right], \tag{A1}$$

in which the parameter σ represents the strength of the disorder. Here, σ can be characterized from the energy broadening δE induced by the interfacial disorder. Using $\delta E = \hbar v_F \sigma$ and the group velocity $v_F = \hbar k_F/m_e$ of free electrons, with k_F being the Fermi wave vector of the metal, we obtain the relation $\sigma/k_F = \delta E/(2E_F)$. We adopt the parameter range $0.01k_F < \sigma < 0.1k_F$ in our calculations. Using $W_{\mathbf{k},\mathbf{k}',\mathbf{q}} = \langle|F_{\mathbf{k},\mathbf{k}',\mathbf{q}}|^2\rangle$ to characterize the strength of interface-induced momentum relaxation, the electrical-injection term reads

$$\partial_t \rho_{\mathbf{q}}|_{\text{inj}} = \frac{\pi}{\hbar}\frac{S}{2N}\frac{a^2}{d^2}\mathcal{J}^2\sum_{\mathbf{k},\mathbf{k}'}\sum_{\zeta,\chi=\uparrow,\downarrow} W_{\mathbf{k},\mathbf{k}',\mathbf{q}}[f_{\mathbf{k}',\zeta}(1-f_{\mathbf{k},\chi})$$
$$\times(\sigma_3+\rho_{\mathbf{q}}) - f_{\mathbf{k},\chi}(1-f_{\mathbf{k}',\zeta})\rho_{\mathbf{q}}]\mathcal{M}_{\zeta\chi}(\mathbf{k},\mathbf{k}') + \text{H.c.}, \tag{A2}$$

where the additional summation over $\mathbf{k}'$ explicitly accounts for the momentum-relaxing scattering channels introduced by interface disorder.

Based on the quantum kinetic equation, we find that the interfacial disorder reduces the spin-current magnitude by $\sim$20% when $\sigma = 0.4/a$, with $a = 0.412$ nm as the lattice constant for Cr_2I_2O. As shown in Fig. 5, stronger disorder leads to a slight reduction of the injected magnon spin current, as the relaxation of momentum conservation redistributes electron-magnon scattering across broader momentum channels and suppresses the injection efficiency into propagating modes.

APPENDIX B: COMPARISON WITH THE THERMALLY DRIVEN TRANSPORT

We compare the distinct properties of magnon spin transport when driven by spin-accumulation and temperature gradients. Thermally driven transport probes only the thermal response, while electrical spin injection directly couples

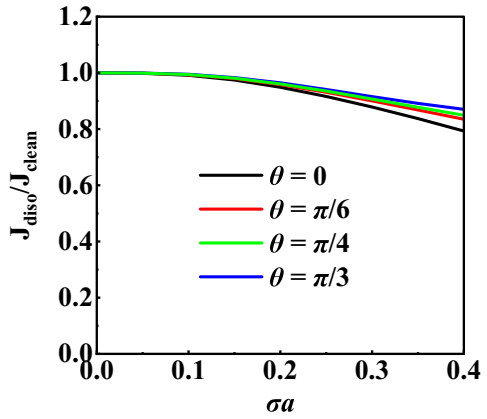


FIG. 5. Ratio of the disorder-affected magnon spin current $J_{\rm diso}$ to $J_{\rm clean}$ in the clean limit ($\sigma \to 0$). a is the lattice constant.

the momentum-dependent magnon spin polarization to the electron spin accumulation. Consequently, the spin response may exhibit a completely different dependence on the relative direction between the Néel vector and the transport direction. To demonstrate this distinction, we calculate the conductivity by the Kubo formula:

$$\sigma^{(1)}_{mn}(\theta) = \frac{\tau_0}{Ak_BT^2}\sum_{\mathbf{k}} v^m_{1,\mathbf{k}}(\theta)v^n_{1,\mathbf{k}}(\theta)\omega_{1,\mathbf{k}}(\theta) \times \frac{e^{\hbar\omega_{1,\mathbf{k}}(\theta)/(k_BT)}}{(e^{\hbar\omega_{1,\mathbf{k}}(\theta)/(k_BT)}-1)^2},$$
$$\sigma^{(2)}_{mn}(\theta) = \frac{\tau_0}{Ak_BT^2}\sum_{\mathbf{k}} v^m_{2,\mathbf{k}}(\theta)v^n_{2,\mathbf{k}}(\theta)\omega_{2,\mathbf{k}}(\theta) \times \frac{e^{\hbar\omega_{2,\mathbf{k}}(\theta)/(k_BT)}}{(e^{\hbar\omega_{2,\mathbf{k}}(\theta)/(k_BT)}-1)^2}, \quad \text{(B1)}$$

where $\{1, 2\}$ labels the two magnon modes, $n = z$ denotes the direction of the temperature gradient, which forms an angle θ with the Néel vector $\mathbf{n}$, and $m = \{x, z\}$ denotes the flow direction. Here, A is the sample area, τ_0 is magnon lifetime, and $v^m_{1/2,\mathbf{k}}(\theta)$ is the group velocity of modes 1 and 2. The longitudinal and transverse spin conductivity tensors read $\sigma^z_\parallel = \hbar(\sigma^{(2)}_{zz} - \sigma^{(1)}_{zz})\cos\theta$, $\sigma^x_\parallel = \hbar(\sigma^{(2)}_{zz} - \sigma^{(1)}_{zz})\sin\theta$, $\sigma^z_\perp = \hbar(\sigma^{(1)}_{xz} + \sigma^{(2)}_{xz})\cos\theta$, and $\sigma^x_\perp = \hbar(\sigma^{(1)}_{xz} + \sigma^{(2)}_{xz})\sin\theta$, in which the superscript indicates the spin-polarization direction.

As shown in Fig. 6, the dependence of the spin conductivity/current on the Néel-vector direction is completely

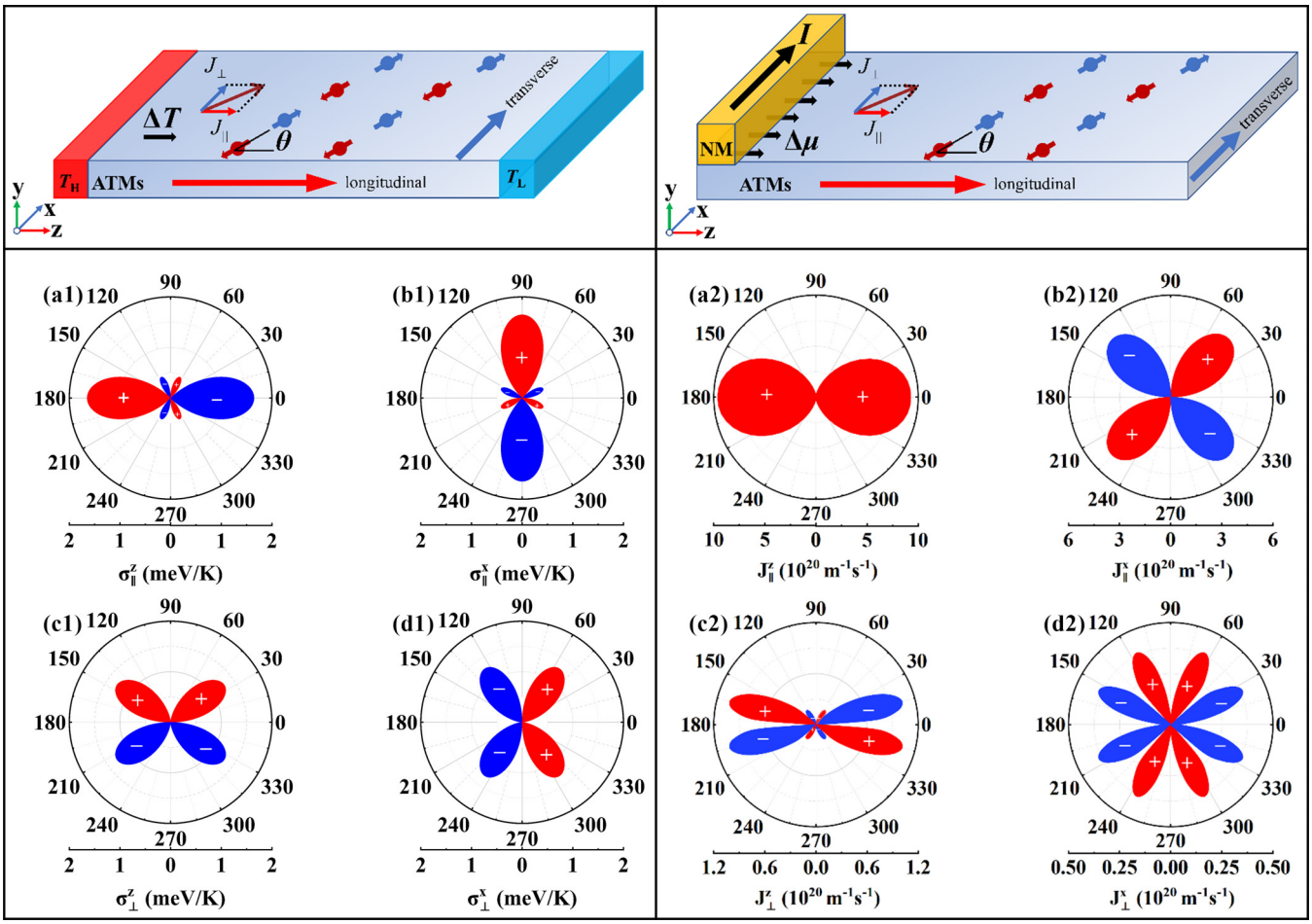


FIG. 6. Néel-vector direction dependence of the spin conductivity/current in the thermal transport [(a1)–(d1), left panel] and electric spin injection [(a2)–(d2), right panel]. In the calculation of the thermal transport, we choose the magnon lifetime $\tau_0 = 1$ ns and the temperature $T = 100$ K. The parameters are chosen from Cr_2I_2O.

different in the thermal transport and electrical spin injection since the thermal gradients probe thermally populated magnon modes, whereas electrical spin injection couples directly to the momentum-dependent magnon spin polarization.

APPENDIX C: CRITERION OF ENHANCEMENT OF TRANSVERSE SPIN CURRENT IN ATMs

The enhancement of transverse spin current in ATMs in comparison to AFMs may depend on material parameters, so a criterion is essential. In uniaxial AFMs, the transverse spin current is generated exclusively by the uniaxial anisotropy K. In ATMs, however, the exchange anisotropy $J_2 \neq J_2'$ induces the band spin splitting, which provides an independent channel for the transverse spin current. Here, the ratio of the exchange anisotropy to the uniaxial anisotropy $|(J_2 - J_2')/K|$ provides a criterion for judging the relative magnitude of the transverse response of uniaxial ATMs and AFMs. As shown in Fig. 7, we compare the longitudinal ($J_\parallel^{\mathrm{ATM}}/J_\parallel^{\mathrm{AFM}}$) and transverse ($J_\perp^{\mathrm{ATM}}/J_\perp^{\mathrm{AFM}}$) spin currents in AFMs and ATMs by continuous variation of J_2' in ATMs with the same material parameters. $|(J_2 - J_2')/K| = 0$ simply corresponds to the uniaxial AFMs. In real materials, it is natural that $|(J_2 - J_2')/K| \sim 100$ since the anisotropy from atomic spin-orbit coupling is usually much weaker than the Coulomb exchange interaction, referring to the ratios for Cr_2I_2O and Cr_2Se_2O that are labeled by blue and red triangles on the curves in Fig. 7. When $|(J_2 - J_2')/K|$ increases from 0 to ∼100, the longitudinal spin current $J_\parallel^{\mathrm{ATM}}/J_\parallel^{\mathrm{AFM}}$ is enhanced slightly [Fig. 7(a)], but transverse spin current $J_\perp^{\mathrm{ATM}}/J_\perp^{\mathrm{AFM}}$ is enhanced by two orders of magnitude [Fig. 7(b)] for both Cr_2I_2O and Cr_2Se_2O.

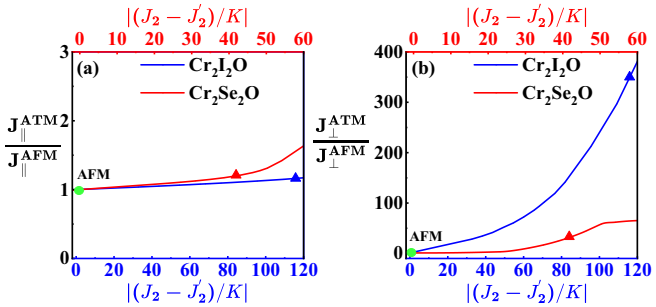


FIG. 7. Ratio of the longitudinal $J_\parallel^{\mathrm{ATM}}/J_\parallel^{\mathrm{AFM}}$ [panel (a)] and transverse $J_\perp^{\mathrm{ATM}}/J_\perp^{\mathrm{AFM}}$ [panel (b)] spin currents in ATMs and AFMs as a function of $|(J_2 - J_2')/K|$ for Cr_2I_2O and Cr_2Se_2O. In the calculations, J_2' is continuously changed without changing the other material parameters in ATMs. We take $\theta = \pi/12$ for proper comparison. The blue and red triangles on the curves indicate the real parameters of Cr_2I_2O and Cr_2Se_2O, respectively.

[1] L. Šmejkal, A. B. Hellenes, R. González-Hernández, J. Sinova, and T. Jungwirth, Giant and tunneling magnetoresistance in unconventional collinear antiferromagnets with nonrelativistic spin-momentum coupling, Phys. Rev. X **12**, 011028 (2022).

[2] L. Šmejkal, J. Sinova, and T. Jungwirth, Beyond conventional ferromagnetism and antiferromagnetism: A phase with nonrelativistic spin and crystal rotation symmetry, Phys. Rev. X **12**, 031042 (2022).

[3] L. Šmejkal, J. Sinova, and T. Jungwirth, Emerging research landscape of altermagnetism, Phys. Rev. X **12**, 040501 (2022).

[4] C. Song, H. Bai, Z. Zhou, L. Han, H. Reichlova, J. H. Dil, J. Liu, X. Chen, and F. Pan, Altermagnets as a new class of functional materials, Nat. Rev. Mater. **10**, 473 (2025).

[5] X. Chen, Y. Liu, P. Liu, Y. Yu, J. Ren, J. Li, A. Zhang, and Q. Liu, Unconventional magnons in collinear magnets dictated by spin space groups, Nature (London) **640**, 349 (2025).

[6] Y. Fukaya, B. Lu, K. Yada, Y. Tanaka, and J. Cayao, Superconducting phenomena in systems with unconventional magnets, J. Phys.: Condens. Matter **37**, 313003 (2025).

[7] T. Jungwirth, J. Sinova, R. M. Fernandes, Q. Liu, H. Watanabe, S. Murakami, S. Nakatsuji, and L. Šmejkal, Symmetry, microscopy and spectroscopy signatures of altermagnetism, Nature (London) **649**, 837 (2026).

[8] O. Amin, A. Dal Din, E. Golias, Y. Niu, A. Zakharov, S. Fromage, C. Fields, S. Heywood, R. Cousins, F. Maccherozzi, *et al.*, Nanoscale imaging and control of altermagnetism in MnTe, Nature (London) **636**, 348 (2024).

[9] A. Hariki, A. Dal Din, O. J. Amin, T. Yamaguchi, A. Badura, D. Kriegner, K. W. Edmonds, R. P. Campion, P. Wadley, D. Backes, L. S. I. Veiga, S. S. Dhesi, G. Springholz, L. Šmejkal, K. Výborný, T. Jungwirth, and J. Kuneš, X-ray magnetic circular dichroism in altermagnetic α-MnTe, Phys. Rev. Lett. **132**, 176701 (2024).

[10] E. Galindez-Ruales, R. Gonzalez-Hernandez, C. Schmitt, S. Das, F. Fuhrmann, A. Ross, E. Golias, A. Akashdeep, L. Lünenbürger, E. Baek, W. Yang, L. Šmejkal, V. Krishna, R. Jaeschke-Ubiergo, J. Sinova, A. Rothschild, C.-Y. You, G. Jakob, and M. Kläui, Revealing the altermagnetism in hematite via XMCD imaging and anomalous Hall electrical transport, Adv. Mater. **37**, e05019 (2025).

[11] J. Krempaský, L. Šmejkal, S. W. D'Souza, M. Hajlaoui, G. Springholz, K. Uhlířová, F. Alarab, P. C. Constantinou, V. Strocov, D. Usanov, *et al.*, Altermagnetic lifting of Kramers spin degeneracy, Nature (London) **626**, 517 (2024).

[12] S. Lee, S. Lee, S. Jung, J. Jung, D. Kim, Y. Lee, B. Seok, J. Kim, B. G. Park, L. Šmejkal, C.-J. Kang, and C. Kim, Broken Kramers degeneracy in altermagnetic MnTe, Phys. Rev. Lett. **132**, 036702 (2024).

[13] S. Reimers, L. Odenbreit, L. Šmejkal, V. N. Strocov, P. Constantinou, A. B. Hellenes, R. Jaeschke Ubiergo, W. H. Campos, V. K. Bharadwaj, A. Chakraborty, T. Denneulin, W. Shi, R. E. Dunin-Borkowski, S. Das, M. Kläui, J. Sinova, and M. Jourdan, Direct observation of altermagnetic band splitting in CrSb thin films, Nat. Commun. **15**, 2116 (2024).

[14] J. Ding, Z. Jiang, X. Chen, Z. Tao, Z. Liu, T. Li, J. Liu, J. Sun, J. Cheng, J. Liu, *et al.*, Large band splitting in g-wave altermagnet CrSb, Phys. Rev. Lett. **133**, 206401 (2024).

[15] R. B. Regmi, H. Bhandari, B. Thapa, Y. Hao, N. Sharma, J. McKenzie, X. Chen, A. Nayak, M. El Gazzah, B. G. Márkus,

L. Forró, X. Liu, H. Cao, J. F. Mitchell, I. I. Mazin, and N. J. Ghimire, Altermagnetism in the layered intercalated transition metal dichalcogenide $CoNb_4Se_8$, Nat. Commun. **16**, 4399 (2025).

[16] F. Zhang, X. Cheng, Z. Yin, C. Liu, L. Deng, Y. Qiao, Z. Shi, S. Zhang, J. Lin, Z. Liu, *et al.*, Crystal-symmetry-paired spin–valley locking in a layered room-temperature metallic altermagnet candidate, Nat. Phys. **21**, 760 (2025).

[17] B. Jiang, M. Hu, J. Bai, Z. Song, C. Mu, G. Qu, W. Li, W. Zhu, H. Pi, Z. Wei, *et al.*, A metallic room-temperature d-wave altermagnet, Nat. Phys. **21**, 754 (2025).

[18] R. González-Hernández, L. Šmejkal, K. Výborný, Y. Yahagi, J. Sinova, T. Jungwirth, and J. Železný, Efficient electrical spin splitter based on nonrelativistic collinear antiferromagnetism, Phys. Rev. Lett. **126**, 127701 (2021).

[19] L. Šmejkal, R. González-Hernández, T. Jungwirth, and J. Sinova, Crystal time-reversal symmetry breaking and spontaneous Hall effect in collinear antiferromagnets, Sci. Adv. **6**, eaaz8809 (2020).

[20] Z. Feng, X. Zhou, L. Šmejkal, L. Wu, Z. Zhu, H. Guo, R. González-Hernández, X. Wang, H. Yan, P. Qin, X. Zhang, H. Wu, H. Chen, Z. Meng, L. Liu, Z. Xia, J. Sinova, T. Jungwirth, and Z. Liu, An anomalous Hall effect in altermagnetic ruthenium dioxide, Nat. Electron. **5**, 735 (2022).

[21] R. D. Gonzalez Betancourt, J. Zubáč, R. Gonzalez-Hernandez, K. Geishendorf, Z. Šobáň, G. Springholz, K. Olejník, L. Šmejkal, J. Sinova, T. Jungwirth, S. T. B. Goennenwein, A. Thomas, H. Reichlová, J. Železný, and D. Kriegner, Spontaneous anomalous Hall effect arising from an unconventional compensated magnetic phase in a semiconductor, Phys. Rev. Lett. **130**, 036702 (2023).

[22] X. Zhou, W. Feng, X. Yang, G.-Y. Guo, and Y. Yao, Crystal chirality magneto-optical effects in collinear antiferromagnets, Phys. Rev. B **104**, 024401 (2021).

[23] I. Gray, Q. Deng, Q. Tian, M. Chilcote, J. S. Dodge, M. Brahlek, and L. Wu, Time-resolved magneto-optical effects in the altermagnet candidate MnTe, Appl. Phys. Lett. **125**, 212404 (2024).

[24] H. Pan, R. Xiao, J. Han, H. Zhu, J. Li, Q. Niu, Y. Gao, and D. Hou, Experimental evidence of Néel-order-driven magneto-optical Kerr effect in an altermagnetic insulator, Phys. Rev. Lett. **136**, 036701 (2026).

[25] X. Zhou, W. Feng, R.-W. Zhang, L. Šmejkal, J. Sinova, Y. Mokrousov, and Y. Yao, Crystal thermal transport in altermagnetic RuO_2, Phys. Rev. Lett. **132**, 056701 (2024).

[26] L. Šmejkal, A. Marmodoro, K.-H. Ahn, R. González-Hernández, I. Turek, S. Mankovsky, H. Ebert, S. W. D'Souza, O. Šipr, J. Sinova, and T. Jungwirth, Chiral magnons in altermagnetic RuO_2, Phys. Rev. Lett. **131**, 256703 (2023).

[27] Q. Cui, B. Zeng, P. Cui, T. Yu, and H. Yang, Efficient spin Seebeck and spin Nernst effects of magnons in altermagnets, Phys. Rev. B **108**, L180401 (2023).

[28] Z. Liu, M. Ozeki, S. Asai, S. Itoh, and T. Masuda, Chiral split magnon in altermagnetic MnTe, Phys. Rev. Lett. **133**, 156702 (2024).

[29] Z. Jin, T. Gong, J. Liu, H. Yang, Z. Zeng, Y. Cao, and P. Yan, Strong coupling of chiral magnons in altermagnets, Phys. Rev. Lett. **135**, 126702 (2025).

[30] Q. Sun, J. Guo, D. Wang, D. L. Abernathy, W. Tian, and C. Li, Observation of chiral magnon band splitting in altermagnetic hematite, Phys. Rev. Lett. **135**, 186703 (2025).

[31] N. Biniskos, M. dos Santos Dias, S. Agrestini, D. Sviták, K.-J. Zhou, J. Pospíšil, and P. Čermák, Systematic mapping of altermagnetic magnons by resonant inelastic x-ray circular dichroism, Nat. Commun. **16**, 9311 (2025).

[32] V. A. S. V. Bittencourt, H. Hosseinabadi, J. Sinova, L. Šmejkal, and J. Marino, Quantum impurity sensing of altermagnetic order, Phys. Rev. Lett. **136**, 146701 (2026).

[33] A. V. Chumak, A. A. Serga, and B. Hillebrands, Magnon transistor for all-magnon data processing, Nat. Commun. **5**, 4700 (2014).

[34] A. V. Chumak, V. I. Vasyuchka, A. A. Serga, and B. Hillebrands, Magnon spintronics, Nat. Phys. **11**, 453 (2015).

[35] P. Pirro, V. I. Vasyuchka, A. A. Serga, and B. Hillebrands, Advances in coherent magnonics, Nat. Rev. Mater. **6**, 1114 (2021).

[36] J. Han, R. Cheng, L. Liu, H. Ohno, and S. Fukami, Coherent antiferromagnetic spintronics, Nat. Mater. **22**, 684 (2023).

[37] J. Chen, H. Yu, R. Gallardo, P. Landeros, and G. Gubbiotti, Magnon confinement and trapping at the nanoscale, Phys. Rep. **1176**, 1 (2026).

[38] K. Wu, J. Dong, M. Zhu, F. Zheng, and J. Zhang, Magnon splitting and magnon spin transport in altermagnets, Chin. Phys. Lett. **42**, 070702 (2025).

[39] E. Galindez-Ruales, W. Yang, T. Dannegger, M. Kundu, J. Köhler, C. Schmitt, F. Fuhrmann, A. Akashdeep, D. M. Tran, X. Ma, G. Jakob, S. Cao, U. Nowak, and M. Kläui, Altermagnetic magnon transport in the d-wave altermagnet $LuFeO_3$, arXiv:2508.14569.

[40] Y. Yang, D. Wang, B. Yang, P. Wang, Y. Mu, Y. Tian, B. Zheng, W. Qin, K. Wang, B. Huang, B. Wang, X. Wan, and D. Wu, Altermagnet-driven magnon spin splitting Nernst effect, Phys. Rev. Lett. **136**, 026701 (2026).

[41] S. M. Wu, W. Zhang, A. KC, P. Borisov, J. E. Pearson, J. Samuel Jiang, D. Lederman, A. Hoffmann, and A. Bhattacharya, Antiferromagnetic spin Seebeck effect, Phys. Rev. Lett. **116**, 097204 (2016).

[42] S. M. Rezende, R. L. Rodríguez-Suárez, and A. Azevedo, Theory of spin Seebeck effects in antiferromagnets, Phys. Rev. B **93**, 014425 (2016).

[43] S. M. Rezende, R. L. Rodríguez-Suárez, and A. Azevedo, Diffusive magnonic spin transport in antiferromagnetic insulators, Phys. Rev. B **93**, 054412 (2016).

[44] W. Lin, K. Chen, S. Zhang, and C. L. Chien, Enhancement of thermally injected spin current through an antiferromagnetic insulator, Phys. Rev. Lett. **116**, 186601 (2016).

[45] R. Cheng, S. Okamoto, and D. Xiao, Spin Nernst effect of magnons in collinear antiferromagnets, Phys. Rev. Lett. **117**, 217202 (2016).

[46] W. Yuan, Q. Zhu, T. Su, Y. Yao, W. Xing, Y. Chen, Y. Ma, X. Lin, J. Shi, R. Shindou, X. C. Xie, and W. Han, Experimental signatures of spin superfluid ground state in canted antiferromagnet Cr_2O_3 via nonlocal spin transport, Sci. Adv. **4**, eaat1098 (2018).

[47] G. R. Hoogeboom and B. J. van Wees, Nonlocal spin Seebeck effect in the bulk easy-plane antiferromagnet NiO, Phys. Rev. B **102**, 214415 (2020).

[48] G. R. Hoogeboom, G.-J. N. S. Nicolaas, A. Alexander, O. Kuschel, J. Wollschläger, I. Ennen, B. J. van Wees, and T. Kuschel, Role of NiO in the nonlocal spin transport through thin NiO films on $Y_3Fe_5O_{12}$, Phys. Rev. B **103**, 144406 (2021).

[49] A. Ross, R. Lebrun, M. Evers, A. Deák, L. Szunyogh, U. Nowak, and M. Kläui, Exceptional sign changes of the nonlocal spin Seebeck effect in antiferromagnetic hematite, Phys. Rev. B **103**, 224433 (2021).

[50] W. Lin, J. He, B. Ma, M. Matzelle, J. Xu, J. Freeland, Y. Choi, D. Haskel, B. Barbiellini, A. Bansil, G. A. Fiete, J. Zhou, and C. L. Chien, Evidence for spin swapping in an antiferromagnet, Nat. Phys. **18**, 800 (2022).

[51] L. Sheng, A. Duvakina, H. Wang, K. Yamamoto, R. Yuan, J. Wang, P. Chen, W. He, K. Yu, Y. Zhang, J. Chen, J. Hu, W. Song, S. Liu, X. Han, D. Yu, S. J.-P. Ansermet, S. Maekawa, D. Grundler, and H. Yu, Control of spin currents by magnon interference in a canted antiferromagnet, Nat. Phys. **21**, 740 (2025).

[52] X. Ye, Q. Cui, W. Lin, and T. Yu, Spin quenching and transport by hidden Dzyaloshinskii-Moriya interactions, Phys. Rev. B **111**, 064401 (2025).

[53] X. Ye and T. Yu, Magnon correlation enables spin injection, dephasing, and transport in canted antiferromagnets, Phys. Rev. B **112**, 224417 (2025).

[54] J. Han, P. Zhang, Z. Bi, Y. Fan, T. S. Safi, J. Xiang, J. Finley, L. Fu, R. Cheng, and L. Liu, Birefringence-like spin transport via linearly polarized antiferromagnetic magnons, Nat. Nanotechnol. **15**, 563 (2020).

[55] T. Wimmer, A. Kamra, J. Gückelhorn, M. Opel, S. Geprägs, R. Gross, H. Huebl, and M. Althammer, Observation of antiferromagnetic magnon pseudospin dynamics and the Hanle effect, Phys. Rev. Lett. **125**, 247204 (2020).

[56] R. Lebrun, A. Ross, O. Gomonay, V. Baltz, U. Ebels, A.-L. Barra, A. Qaiumzadeh, A. Brataas, J. Sinova, and M. Kläui, Long-distance spin-transport across the Morin phase transition up to room temperature in ultra-low damping single crystals of the antiferromagnet α-Fe_2O_3, Nat. Commun. **11**, 6332 (2020).

[57] R. Lebrun, A. Ross, S. A. Bender, A. Qaiumzadeh, L. Baldrati, J. Cramer, A. Brataas, R. A. Duine, and M. Kläui, Tunable long-distance spin transport in a crystalline antiferromagnetic iron oxide, Nature (London) **561**, 222 (2018).

[58] D. K. de Wal, R. L. Mena, M. Zohaib, and B. J. van Wees, Gate control of magnon spin transport in unconventional magnon transistors based on the van der Waals antiferromagnet $CrPS_4$, Phys. Rev. B **110**, 224434 (2024).

[59] L. J. Cornelissen, J. Liu, B. J. van Wees, and R. A. Duine, Spin-current-controlled modulation of the magnon spin conductance in a three-terminal magnon transistor, Phys. Rev. Lett. **120**, 097702 (2018).

[60] W. Lin, Magnetization reversal, and generation and detection of pure spin-current, Ph.D. thesis, Nanjing University, 2007.

[61] L. J. Cornelissen, J. Liu, R. A. Duine, J. Ben Youssef, and B. J. van Wees, Long-distance transport of magnon spin information in a magnetic insulator at room temperature, Nat. Phys. **11**, 1022 (2015).

[62] See Supplemental Material at http://link.aps.org/supplemental/10.1103/4mcl-jtty for the calculation of magnon modes, a detailed discussion of the quantum kinetic equation, and the symmetry operation on the response tensors.

[63] H. Zhu, J. Li, X. Chen, Y. Yu, and Q. Liu, Magnetic geometry induced quantum geometry and nonlinear transports, Nat. Commun. **16**, 4882 (2025).

[64] S. S.-L. Zhang and S. Zhang, Spin convertance at magnetic interfaces, Phys. Rev. B **86**, 214424 (2012).

[65] N. Rohling, E. L. Fjærbu, and A. Brataas, Superconductivity induced by interfacial coupling to magnons, Phys. Rev. B **97**, 115401 (2018).

[66] E. Thingstad, E. Erlandsen, and A. Sudbø, Eliashberg study of superconductivity induced by interfacial coupling to antiferromagnets, Phys. Rev. B **104**, 014508 (2021).

[67] P. Tang and G. E. W. Bauer, Electrical injection and transport of coherent magnon superposition states in noncollinear antiferromagnets, Phys. Rev. B **112**, L180406 (2025).

[68] K. Sourounis and A. Manchon, Efficient generation of spin currents in altermagnets via magnon drag, Phys. Rev. B **111**, 134448 (2025).

[69] S. Das, A. Ross, X. X. Ma, S. Becker, C. Schmitt, F. van Duijn, E. F. Galindez-Ruales, F. Fuhrmann, M.-A. Syskaki, U. Ebels, V. Baltz, A.-L. Barra, H. Y. Chen, G. Jakob, S. X. Cao, J. Sinova, O. Gomonay, R. Lebrun, and M. Kläui, Anisotropic long-range spin transport in canted antiferromagnetic orthoferrite $YFeO_3$, Nat. Commun. **13**, 6140 (2022).

[70] H. Wang, R. Yuan, Y. Zhou, Y. Zhang, J. Chen, S. Liu, H. Jia, D. Yu, J.-P. Ansermet, C. Song, and H. Yu, Long-distance coherent propagation of high-velocity antiferromagnetic spin waves, Phys. Rev. Lett. **130**, 096701 (2023).

[71] A. T. Costa, J. C. G. Henriques, and J. Fernández-Rossier, Giant spatial anisotropy of magnon Landau damping in altermagnets, SciPost Phys. **18**, 125 (2025).

[72] T. Osumi, S. Souma, T. Aoyama, K. Yamauchi, A. Honma, K. Nakayama, T. Takahashi, K. Ohgushi, and T. Sato, Observation of a giant band splitting in altermagnetic MnTe, Phys. Rev. B **109**, 115102 (2024).

[73] D. Qu, S. Y. Huang, B. F. Miao, S. X. Huang, and C. L. Chien, Self-consistent determination of spin Hall angles in selected 5*d* metals by thermal spin injection, Phys. Rev. B **89**, 140407(R) (2014).

[74] L. J. Cornelissen, K. J. H. Peters, G. E. W. Bauer, R. A. Duine, and B. J. van Wees, Magnon spin transport driven by the magnon chemical potential in a magnetic insulator, Phys. Rev. B **94**, 014412 (2016).

[75] R. S. Nair, M. S. Rang, and P. J. Kelly, Spin Hall effect in a thin Pt film, Phys. Rev. B **104**, L220411 (2021).

[76] P. Wei, S. Lee, F. Lemaitre, L. Pinel, D. Cutaia, W. Cha, F. Katmis, Y. Zhu, D. Heiman, J. Hone, J. S. Moodera, and C.-T. Chen, Strong interfacial exchange field in the graphene/EuS heterostructure, Nat. Mater. **15**, 711 (2016).

[77] J. M. Gomez-Perez, X.-P. Zhang, F. Calavalle, M. Ilyn, C. González-Orellana, M. Gobbi, C. Rogero, A. Chuvilin, V. N. Golovach, L. E. Hueso, F. S. Bergeret, and F. Casanova, Strong interfacial exchange field in a heavy metal/ferromagnetic insulator system determined by spin Hall magnetoresistance, Nano Lett. **20**, 6815 (2020).

[78] S. A. Bender, H. Skarsvåg, A. Brataas, and R. A. Duine, Enhanced spin conductance of a thin-film insulating antiferromagnet, Phys. Rev. Lett. **119**, 056804 (2017).

[79] R.-C. Xiao, H. Li, H. Han, W. Gan, M. Yang, D.-F. Shao, S.-H. Zhang, Y. Gao, M. Tian, and J. Zhou, Anomalous-Hall Néel textures in altermagnetic materials, Sci. China Phys. Mech. Astron. **69**, 217511 (2026).

[80] R.-C. Xiao, Y. Jin, Z.-F. Zhang, Z.-H. Feng, D.-F. Shao, and M. Tian, TensorSymmetry: A package to get symmetry-adapted tensors disentangling spin-orbit coupling effect and establishing analytical relationship with magnetic order, Comput. Phys. Commun. **318**, 109872 (2026).

[81] M. S. Heydari, W. Belzig, and N. Rohling, Influence of disorder at insulator-metal interface on spin transport, Phys. Rev. B **111**, 054414 (2025).